SEGMENTATION OF RETINAL BLOOD VESSELS USING A NOVEL FUZZY LOGIC ALGORITHM

Burak YILDIRIM

Under the Supervision of Dr. Buket D. BARKANA

MASTER'S THESIS

SUBMITTED IN PARTIAL FULFILMENT OF THE REQUIREMENTS FOR THE DEGREE OF MASTER OF SCIENCE IN THE DEPARTMENT OF ELECTRICAL ENGINEERING

THE SCHOOL OF ENGINEERING

UNIVERSITY OF BRIDGEPORT

CONNECTICUT, USA 06604

May 2015

SEGMENTATION OF RETINAL BLOOD VESSELS

USING A NOVEL FUZZY LOGIC ALGORITHM

APPROVALS

Committee Members

Name	**Signature**	**Date**
Dr. Buket D. Barkana	_____	_____
Dr. Navarun Gupta	_____	_____
Dr. Miad Faezipour	_____	_____

SEGMENTATION OF RETINAL BLOOD VESSELS USING A NOVEL FUZZY LOGIC ALGORITHM

ABSTRACT

In this work, a rule-based method is presented for blood vessel segmentation in digital retinal images. This method can be used in computer analyses of retinal images, e.g., in automated screening for diabetic retinopathy. Diabetic retinopathy is the most common diabetic eye disease and a leading cause of blindness. Diagnosis of diabetic retinopathy at an early stage can be done through the segmentation of the blood vessels of retina. Many studies have been carried out in the last decade in order to obtain accurate blood vessel segmentation in retinal images including supervised and rule-based methods.

This method uses eight feature vectors for each pixel. These features are means and medians of intensity values of pixel itself, first and second nearest neighbor at four directions. Features are used in fuzzy logic algorithm as crisp input. The final segmentation is obtained using a thresholding method. The method was tested on the publicly available database DRIVE and its results are compared with distinguished published methods. Our method achieved an average accuracy of 93.82% and an area under the receiver operating characteristic curve of 94.19% for DRIVE database. Our results demonstrated an average sensitivity of 72.28% and a specificity of 97.04%. The calculated sensitivity and specificity

values for DRIVE database also state that the proposed segmentation method is effective and robust.

ACKNOWLEDGEMENTS

I would like to express my sincere gratitude to my advisor Dear Buket D. Barkana for giving me the opportunity to research and work with her. Without her guidance and persistent help, this thesis would not have been possible.

I would also like to thank my committee member and department's chair, Dear Navarun Gupta for giving financial support to me in order to buy equipment.

I owe a deep sense of gratitude to my committee member Dear Miad Faezipour who gave me the chance to study in her research laboratory and helping me to develop my skills.

I would also like to thank the authors of DRIVE databases for making their data publicly available.

In addition, I thank to my grantor, Republic of Turkey, Ministry of National Education for funding me to complete my masters' education from beginning to end.

TABLE OF CONTENTS

LIST OF TABLES

LIST OF FIGURES

LIST OF ABBREVIATIONS

AHE	Adaptive histogram equalization
AMD	Age related macular degeneration
AUC	Area under curve
DR	Diabetic retinopathy
DRIVE	Digital retinal image for vessel extraction
FIS	Fuzzy inference system
FOV	Field of view
FPF	False positive fraction
kNN	K^{th} nearest neighbor
MF	Membership function
ANN	Artificial neural network
RGB	Red-green-blue
ROC	Receiver operating characteristic curve

ROI	Region of interest
SVM	Support vector machine
TPF	True positive fraction

CHAPTER 1: INTRODUCTION

Digital retinal imaging has an important role to analyze eye diseases such as diabetic retinopathy, glaucoma, and age-related macular degeneration. They are known as the most prevalent causes of blindness in the world. An analysis of retinal images can have applications in a wide range of fields, including retinal vascular segmentation, optic nerve segmentation, and retinal disease screening [1].

Diabetic retinopathy (DR) is the result of damage to the blood vessels in the retina. In some people with DR, blood vessels may swell and leak fluid. In other people, abnormal new blood vessels grow on the surface of the retina [2]. It is a major cause of visual impairment, and is the leading cause of blindness. The number of people diagnosed with this disease is rapidly increasing in the US and the world. DR is classified as a vascular disorder since most of the clinically visible lesions of DR are vascular in nature. Retinopathy has two stages: An early, nonproliferative stage and an advanced, proliferative or neovascular stage. The early, nonproliferative stage of the retinopathy is characterized by damaged small retinal blood vessels and rarely has clinical significance but the amount and severity of the changes in this stage provide clues about the progress toward the advance stage of the disease. It is reported that patients with early DR typically have retinal microaneurysms that are swelled damaged blood vessels. Microaneurysms appear as red

dots on dilated funduscopic examination. These microaneurysms may leak fluid leading to swelling, bleeding, and eventually vision loss. The advanced, neovascular stage of the retinopathy is characterized by retinal neovascular events and impairment of vision [3]. A comparison normal image with DR image is shown in Fig.1 (a), and (b), respectively.

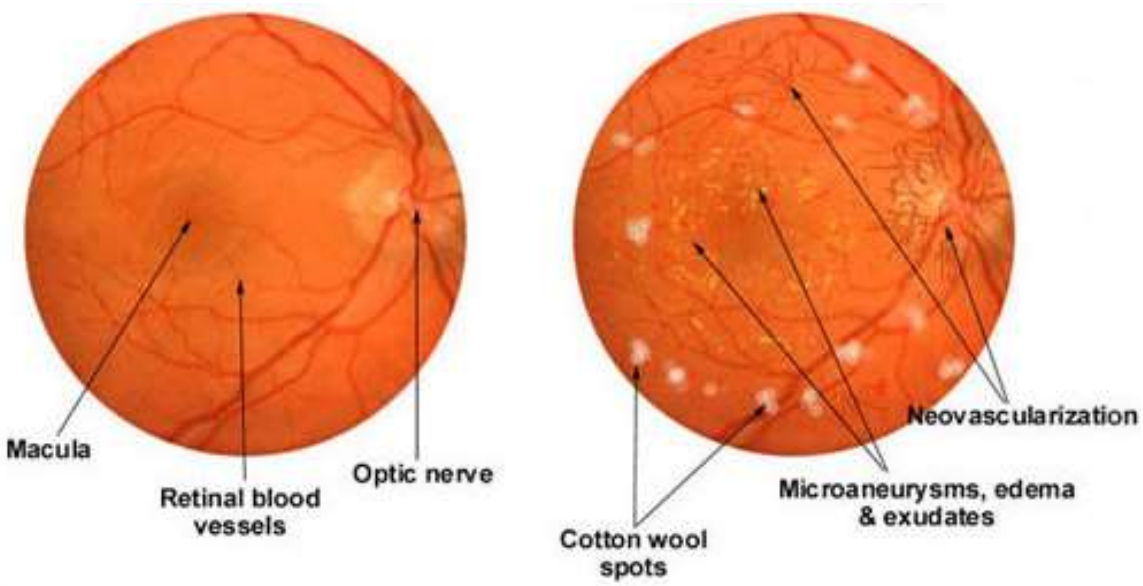

(a) (b)

Figure 1 *A comparison of (a) Healty eye image, and (b) Diabetic retinopathy image by courtesy of [4]*

Diabetic retinopathy (DR) originates from the consequences of high sugar level in blood (hyperglycemia). People with diabetes mellitus have a high risk of vision loss since DR damages retinal vessels [5]. DR stimulates ischemia, a growth of new blood vessels that may subsequently bleed or cause retinal detachment, and breakdown of the blood-

retinal barrier that is leading to fluid leakage, diabetic macular edema, and damage to photoreceptors [6].

Age-related macular degeneration (AMD) is another main source of irreversible visual loss in the center of visual field. It is usually seen in older people [7]. It causes damage to the macula, a small spot near the center of the retina and the part of the eye needed for sharp, central vision, which lets us see objects that are straight ahead. AMD by itself does not lead to complete blindness, with no ability to see. However, the loss of central vision in AMD can interfere with simple everyday activities, such as the ability to see faces, drive, read, write, or do close work, such as cooking or fixing things around the house [8]. A sample age-related macular degeneration image is shown in Fig.2.

Figure 2 A sample image of age related macular degeneration by courtesy of [9]

Intraocular pressure is a major risk factor for optic nerve damage and causes vision loss that is named as glaucoma. A study led by Mitchell *et al.* reported that retinal blood vessels unusually shrink in the initial period of open-angle glaucoma [10]. It is encouraged that a computer-based imaging tool designed to detect narrowing of the retinal artery diameter could effectively identify those who are at risk for open-angle glaucoma. [11]. Images for stages of glaucoma development are shown in Fig.3.

(a) (b) (c)

Figure 3 *Development images of glaucoma by courtesy of [12] (a) "Healthy eye" Flow of aqueous humour through the drainage canal. (b) Drainage canal blocked; build up of fluid. (c) "Glaucoma" Increased pressure damages blood vessels and optic nerve.*

The measurements of vessel features, such as length, width, color, tortuosity, reflectivity and branching pattern, among others, can provide new insights to diagnose and stage pathologies which affect the morphological and functional characteristics of blood vessels. However, when the vascular network is complex, or the number of vessels in an image is large, manual delineation can become tedious or even impossible. A feasible solution is the use of automated analysis, which is nowadays commonly accepted by the

medical community [13]. Retinal vascular segmentation can reveal the details in identifying and treating causes of vision loss. For eye diseases, the segmentation of vessel structure can be helpful for early detection and treatment to prevent vision loss by analyzing the changes in blood vessels.

CHAPTER 2: LITERATURE SURVEY

Many different approaches for vessel segmentation have been proposed in the literature. They can be divided into two groups. The first group consists of rule-based methods including vessel tracking [14] [15], matched filtering [16] [17] [18], mathematical morphology [13] [19], or multi-threshold probing [20]. The second group consists of supervised methods that based on pixel classification and require manually labeled images for training.

2.1 Rule-based Methods

In rule-based methods, the training data or hand-labeled ground truths do not contribute directly to the design of the algorithm. Vessel tracking algorithms follow vessel centerlines from an initial point located manually or automatically. These algorithms only evaluate pixels close to the vasculature, looking for its local information. Gagnon *et al.* [14] proposed a vessel tracking method which uses recursive dual edge tracking and connectivity recovering. Their method looks at the borders of vessel and the connectivity of twin border after detecting its edge information by using canny edge operator. Chaudhuri *et al.* [16] introduced two-dimensional match filters based on the optical and spatial properties of blood vessels. They used 12 rotated templates of a 2-D Gaussian shaped curve

in order to search for vessel segments at all possible directions. Their method achieved average accuracy of 87.73% for DRIVE database. Li *et al*. [18] proposed a simple and efficient multiscale vessel extraction scheme by multiplying the responses of matched filters at three scales. Mendoça and Campilho [13] used a combination of morphological operations and nonlinear filters. Their algorithm starts with the extraction of vessel centerlines and connects them with four directional differential operators. Then, the vascular network is segmented from the background by applying morphological methods. They reported the highest average accuracy as 94.63% for DRIVE database among the rule-based methods. Jiang *et al.* [20] presented a general framework of model-based locally adaptive thresholding. It is based on multi-threshold probing scheme. Combining shape, color/intensity, and contrast information of retinal vessels into the verification procedure performs knowledge-guided adaptive thresholding. Martinez-Perez *et al.* [21] proposed a method based on multi-scale feature extraction. Features obtained from the first and second spatial derivatives of the intensity image are used in a multiple pass region growing procedure, which segments the retinal vessels progressively. They achieved the average accuracy of 93.44% for DRIVE database. Tolias *et al*. [22] proposed a fuzzy vessel tracking algorithm and used a fuzzy C-means clustering algorithm to decide if regions were vessel or non-vessel. They reported the overall performance of their algorithm as 82.35% by using only three retinal fundus images. Their unsupervised vessel segmentation method overcomes the initialization problem that is encountered in the literature. Rahman *et al*. [23] proposed a fuzzy rule-based method for detecting the center of the fovea and its boundary in a fundus image. Cemal and Iki [24] proposed an alternate personal

identification system based on retinal vascular network in retinal images, which tolerates scale, rotation and translation in comparison.

2.2 Supervised Methods

In supervised methods, rules for vessel segmentation are learned by the algorithm in terms of a training set. So they require ground truth segmentation for training before computation. Supervised methods categorize pixels into two group, vessel or non-vessel, by using a feature vector. Niemeijer *et al.* [25] presented a K-nearest neighbor (kNN) classifier, where k is 30. The feature vector contained the Gaussian and its derivatives up to order 2 at 5 different scales (s = 1, 2, 4, 8, 16 pixels), augmented with the green channel of the original image. 94.16% is reported as average accuracy using DRIVE database. Staal *et al*. [26] have proposed a supervised method that is based on the extraction of image ridges. The ridges were used to compose primitives in the form of line elements. Retinal image was subsequently partitioned into patches due to assigning each pixel to the nearest line element. For every pixel, feature vectors were computed and were classified by using a kNN classifier and sequential forward feature selection. Their method achieved average accuracy of 94.41% for DRIVE database. Sinthanayothin *et al.* [27] used a multilayer perceptron neural network method whose features are constructed using principal component analysis of the image and edge detection for the first principal component. Soares *et al.* [28] used a Gaussian mixture model Bayesian classifier. Feature vector is constructed by a multiscale analysis that was performed on the image using two-dimensional the Gabor wavelet transform. As pixel features, the grey-level of the inverted

green channel of original image and the maximum Gabor transform response over angles at four different scales were considered. The average accuracy of their method was reported as 94.66% for DRIVE database. Ricci and Perfetti [29] achieved a high average accuracy rate (95.95% for DRIVE database) by using support vector machine (SVM) and a feature vector that is prepared by two orthogonal line detectors along with the grey-level of the target pixels. Gardner *et al.* [30] used a back propagation neural network (NN) classifier. After images divided into blocks of 30x30 and 20x20 pixels, depending on features detected, training data were used to teach to classify the blocks as vessel or non-vessel. Marin *et al.* [31] proposed a neural network (NN) scheme for pixel classification and computes a 7-D vector composed of gray-level and moment invariants-based features for pixel representation. Fraz *et al*. [32] used an ensemble system of bagged and boosted decision trees. Their method utilizes a feature vector based on the orientation analysis of gradient vector field, morphological transformation, line strength measures, and Gabor filter responses.

CHAPTER 3: METHODOLOGY

The proposed method includes four main stages which are (1) pre-processing (2) feature extraction (3) fuzzy logic algorithm, and (4) post-processing. Fig.4 shows all stages of this work. In the pre-processing stage, green channel extraction, adaptive histogram equalization (AHE), background extraction, creating normalized image and masking are implemented. In the third section, fuzzy sets and rules are created, and extracted features in second section are evaluated. Thresholding is performed in the post-processing stage.

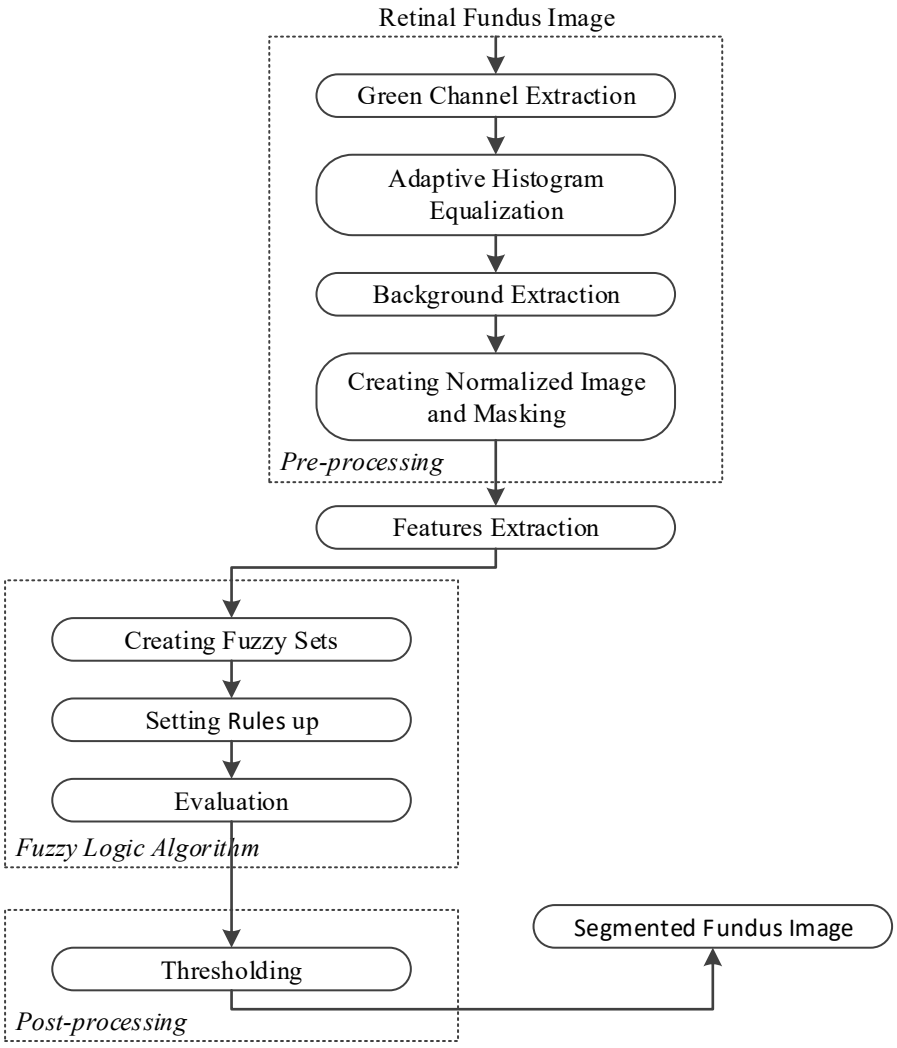

Figure 4 Block diagram of the proposed method

3.1. Pre-processing

Retinal images may have poor contrast and noisy backgrounds. Hence, the images need to be enhanced before any segmentation method. Here, pre-processing stage performs green channel extraction and adaptive histogram equalization (AHE) to enhance the contrast level of the image by uniformly spreading the image intensity levels.

Fig.5 (a) shows an original retinal image that has red-green-blue (RGB) channels. The green channel of retinal images provides more details about the vessel structure, while the red channel is the brightest color channel and has low contrast, and the blue channel offers poor dynamic range [33]. Therefore, the green channel of retinal image, shown in Fig.5 (b), is used in this work.

(a) (b) (c)

Figure 5 *(a) Original retinal image (Image 19), (b) Green channel image, (c) Complement of the green channel image*

AHE [34] is applied to the complement of the green channel image (Fig.5 (c)) in order to enhance the contrast. AHE processes on small areas instead of the entire image, so the enhancement is taken shape for each of these areas individually [35]. Fig.6 (a) shows the image after AHE was applied.

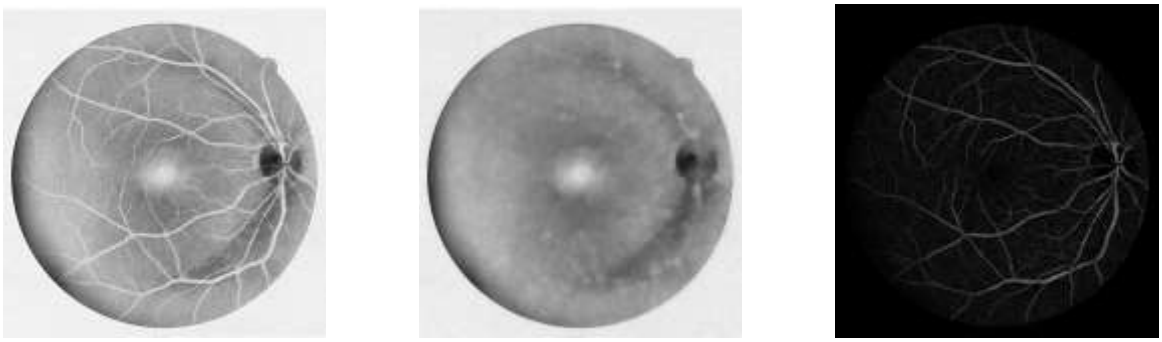

(a) (b) (c)

Figure 6 *(a) Adaptive histogram equalization image (AHE), (b) Background image, (c) Normalized and masked image.*

Morphological operations are used to create a uniform background image [36]. As it can be seen in the Fig.6 (a) the background became non-uniform after the AHE stage while the vessel structure got a better contrast. The most basic morphological operations are erosion and dilation. Erosion trims pixels on object boundaries, while dilation adds pixels to the boundaries of objects in the digital images. The number of pixels trimmed from or added to objects in the image depends on a structuring element. The structuring element is known as a matrix with values 1 and 0 only, and takes different shapes and sizes with respect to the application [37].

The dilation of the erosion is called opening morphology that is defined by Eq.1.

$$A^{\circ}B = (A \ominus B) \oplus B \quad (1)$$

where, $A^{\circ}B$ refers to the morphological opening process of image A with a structuring element B, and $\ominus$ and $\oplus$ refer to erosion and dilation, respectively.

In order to generate a background image, I_{BK}, the blood vessels are suppressed by an opening morphological operation with a *non-flat and ball-shaped structuring element whose radius in the X-Y plane is 6 and whose height is 6.* This background is subtracted from the result of the adaptive histogram equalization, I_{AHE}, so as to obtain a normalized image, I_{NR}.

$$I_{NR}(i,j) = \text{masking}\{I_{AHE}(i,j) - I_{BK}(i,j)\} \quad (2)$$

where i and j are pixel coordinates. The normalized image is found by Eq.2. Masking is applied to remove the residual outside the fundus region of interest (ROI) in the entire image. The background and I_{NR} normalized image can be seen in Fig.6 (b) and (c), respectively.

3.2. Features Extraction

In this work, means and medians of intensity values of five pixels (pixel itself, first and second nearest neighbor) are calculated at four directions: horizontal, vertical, up diagonal, and down diagonal as features. Fig.7 demonstrates these features. The processed pixel is represented as in red and its neighbors are represented as in yellow. Features; F1, F2, F3, and F4 are calculated as the mean values and F5, F6, F7, and F8 are calculated as the median values of the corresponding pixels.

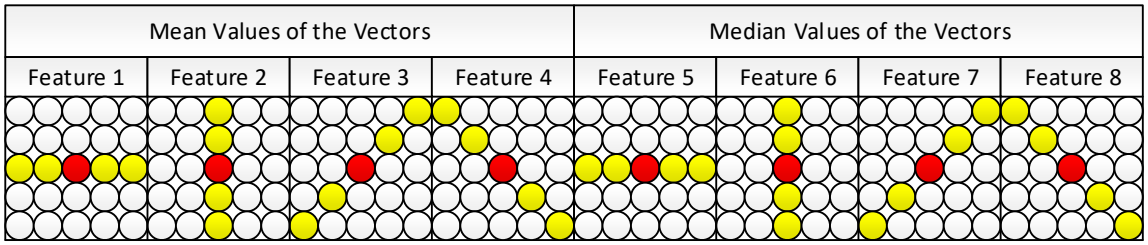

Figure 7 Features extraction for inputs of the fuzzy logic system

These eight features are defined as:

$$F1_{ij} = mean\{I_{NR}(i-2,j), I_{NR}(i-1,j), I_{NR}(i,j), I_{NR}(i+1,j), I_{NR}(i+2,j)\} \quad (3)$$

$$F2_{ij} = mean\{I_{NR}(i,j-2), I_{NR}\ (i,j-1), I_{NR}(i,j), I_{NR}(i,J+1), I_{NR}(i,j+2)\} \quad (4)$$

$$F3_{ij} = mean\{I_{NR}(i-2,j-2), I_{NR}(i-1,j-1), I_{NR}(i,j), I_{NR}(i+1,j+1), I_{NR}(i+2,j+2)\} \quad (5)$$

$$F4_{ij} = mean\{I_{NR}(i-2,j+2), I_{NR}(i-1,j+1), I_{NR}(i,j), I_{NR}(i+1,j-1), I_{NR}(i+2,j-2)\} \quad (6)$$

$$F5_{ij} = median\{I_{NR}(i-2,j), I_{NR}(i-1,j), I_{NR}(i,j), I_{NR}(i+1,j), I_{NR}(i+2,j)\} \quad (7)$$

$$F6_{ij} = median\{I_{NR}(i,j-2), I_{NR}\ (i,j-1), I_{NR}(i,j), I_{NR}(i,J+1), I_{NR}(i,j+2)\} \quad (8)$$

$$F7_{ij} = median\{I_{NR}(i-2,j-2), I_{NR}(i-1,j-1), I_{NR}(i,j), I_{NR}(i+1,j+1), I_{NR}(i+2,j+2)\} \quad (9)$$

$$F8_{ij} = median\{I_{NR}(i-2,j+2), I_{NR}(i-1,j+1), I_{NR}(i,j), I_{NR}(i+1,j-1), I_{NR}(i+2,j-2)\} \quad (10)$$

where I_{NR} is the normalized image and i and j are the pixel coordinates in the FOV. These eight features are used as crisp inputs for input membership functions in the fuzzy logic system. In order to analyze features for vessel and non-vessel pixels discretely, histogram, a graphical representation of the distribution of data, are plotted. Fig.8 shows the distributions of vessels and non-vessels pixels for F1. As it can be seen, there is an

overlapping regions of two distributions. This overlapping area shows that vessels and non-vessels pixels may carry same intensity value.

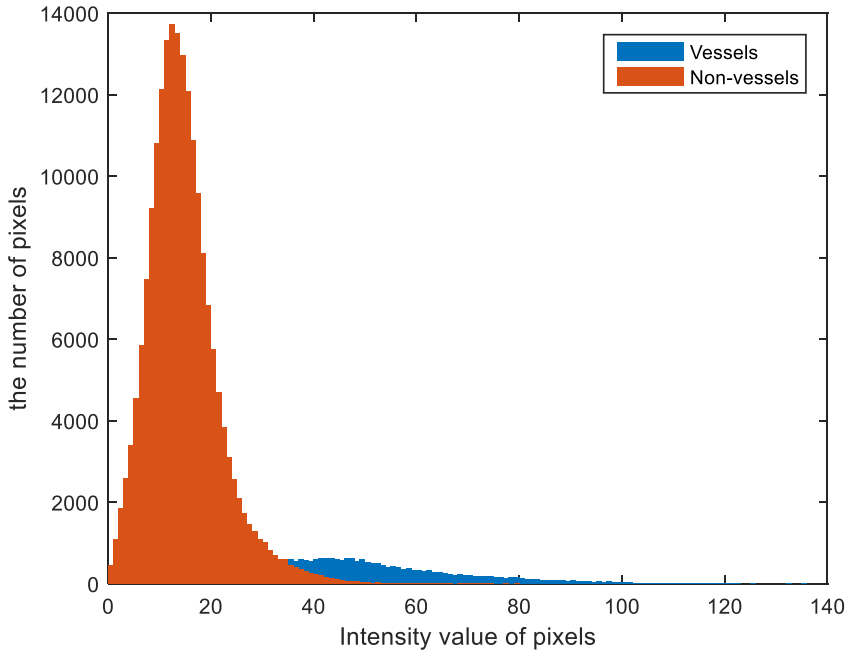

Figure 8 *Frequency distributions of intensity value of vessels and non-vessels for F1.*

L-moments (skewness and kurtosis) are an alternative system for describing the shape of a probability distributions [38]. Skewness is a measure of symmetry, or more precisely, the lack of symmetry while kurtosis is a measure of whether the data are peaked or flat relative to a normal distribution. The skewness of a distribution is defined as:

$$s = \frac{\sum_{i=1}^{N}(x_i-\mu)^3/N}{\sigma^3} \tag{11}$$

where μ is the mean of x, σ is the standard deviation of x, *N* is the number of data points. The kurtosis of a distribution is defined as:

$$k = \frac{\sum_{i=1}^{N}(x_i-\mu)^4/N}{\sigma^4} \quad (12)$$

where μ is the mean of x, σ is the standard deviation of x, *N* is the number of data points. L-moments statistical profile of all features is calculated for vessel and non-vessel pixels, and is given in Table.1.

Table 1 *Statistical Analysis of All Features by Mean, Standard Deviation, Skewness and Kurtosis*

Class		F1	F2	F3	F4	F5	F6	F7	F8
Vessel	Mean	42.989	43.999	40.700	41.104	44.565	45.440	42.162	42.573
	Std	21.491	22.350	19.989	21.486	23.972	24.399	23.612	24.284
	Skewness	1.046	0.877	0.900	1.178	0.852	0.789	0.874	0.929
	Kurtosis	4.578	3.940	4.007	4.932	3.862	3.704	3.789	3.935
Non-vessel	Mean	14.164	14.005	14.486	14.421	13.646	13.595	13.740	13.717
	Std	6.934	7.322	6.999	6.881	7.304	7.730	7.153	7.151
	Skewness	1.356	1.181	1.494	1.380	1.158	1.067	1.221	1.181
	Kurtosis	7.322	6.406	8.048	7.514	7.029	6.297	7.890	7.480

The skewness of the normal distribution is zero. If skewness is negative, the data are spread out more to the left of the mean than to the right. If skewness is positive, the

data are spread out more to the right. The kurtosis for a normal distribution is three. Distributions that are more outlier-prone than the normal distribution have kurtosis greater than three; distributions that are less outlier-prone have kurtosis less than three.

3.3. Fuzzy Logic System

The theory of fuzzy sets was introduced by Lotfi A. Zadeh in 1965 [39]. A fuzzy set is a class of objects. The sets are characterized by a membership function that assigns to each object a degree of membership between zero and one. By means of this characteristic, fuzzy logic techniques give more satisfactory results than conventional mathematical models for complex and uncertain systems. In recent years, the use of fuzzy logic technique has been a very popular method in many areas such as control systems, robotics and noise recognition algorithms [40]. It can also be successful in the area of image processing [41].

There are four principal elements for a fuzzy system: fuzzifier, fuzzy rule base, fuzzy inference engine, and defuzzifier [42]. Basic configuration of fuzzy systems is shown in Fig.9. The fuzzifier performs a mapping from the crisp input to fuzzy set. The input that is characterized by a membership function. The fuzzy rule base consists of a set of linguistic rules in the form of "*IF a set of conditions are satisfied, THEN a set of consequences are inferred.*" The fuzzy inference engine is decision-making logic that employs fuzzy rules from the fuzzy rule bases to determine a mapping from the fuzzy sets in the input space to the fuzzy set in the output space [43]. The defuzzifier performs a mapping from the fuzzy set in the output to crisp output.

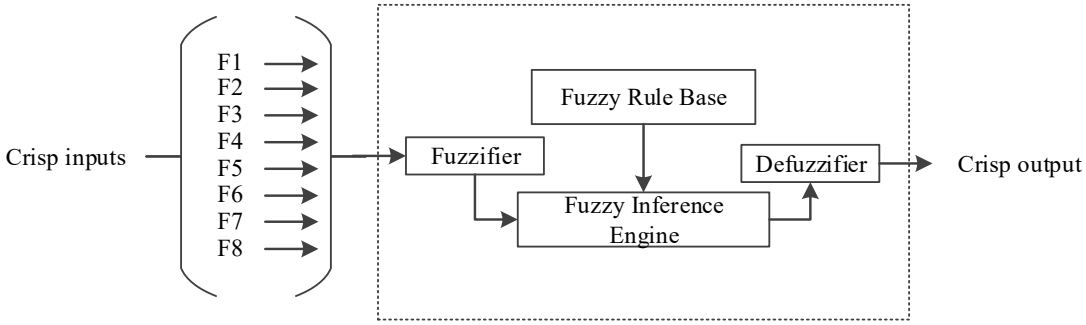

Figure 9 Basic configuration of fuzzy logic systems

There are two different types of fuzzy inference systems (FIS): Takagi-Sugeno [44] and Mamdani [45]. The main difference between them is that the output membership function of Takagi-Sugeno could either be constant or linear mathematical expression while the output membership function of Mamdani is a fuzzy set. In this study, Mamdani fuzzy inference system is preferred because it is intuitive and well suited to human input. A Mamdani FIS was created by using MATLAB command window as seen in Fig.10.

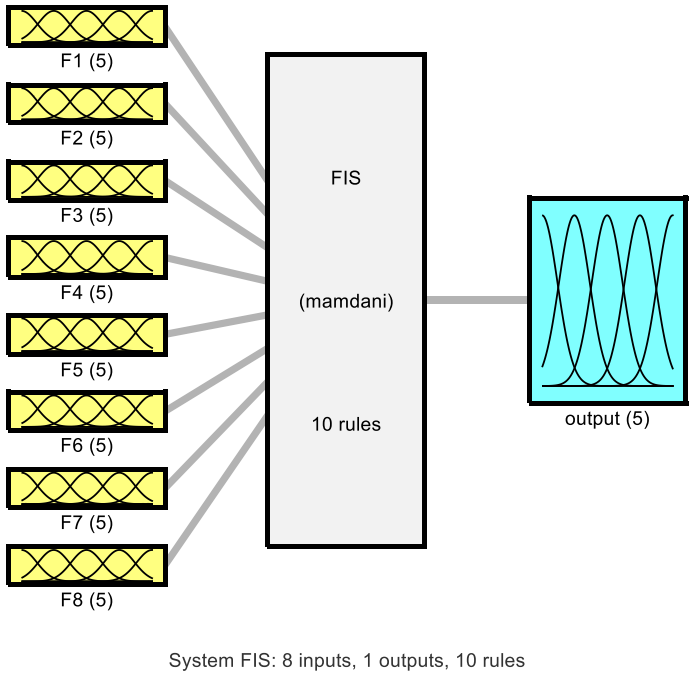

Figure 10 Mamdani fuzzy inference system (FIS)

The process of fuzzy inference includes three sections: membership functions, IF-THEN rules, and logical operations. IF X is a collection of objects denoted generally by x THEN a fuzzy set A in X is a set of ordered pairs:

$$A = \{(x,\mu_{\mathrm{A}}(x))|x \in X\} \tag{13}$$

where $\mu_{\mathrm{A}}(x)$ is called the membership function for the fuzzy set A [46]. There are different shapes of fuzzy membership functions (MF) such as triangle, trapezoidal, Gaussian, and sigmoidal as seen in Fig.11.

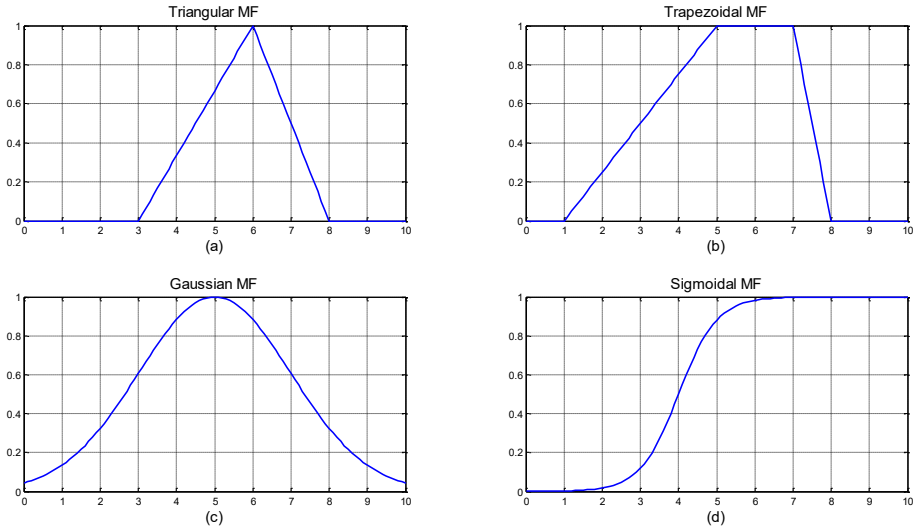

Figure 11 Plots of four parameterized MFs: (a) triangle(x;3,6,8); (b) trapezoid(x;1,5,7,8); (c) Gaussian(x;2,5); (d) sigmoid(x;2,4)

The simplest MFs are formed using straight lines. Of these, the simplest is the triangular MF. This function is nothing more than a collection of three points forming a triangle. The trapezoidal MF has a flat top and really is just a truncated triangle curve. These straight line membership functions have the advantage of simplicity. A triangular MF is specified by three parameters a, b, and c as follows:

$$\mu_A(x; a, b, c) = \max(\min\left(\frac{x-a}{b-a}, \frac{c-x}{c-b}\right), 0) \quad (14)$$

where $\mu_A(x)$ is the membership function. The parameters a and c locate the *feet* of the triangle and the parameter b locates the *peak*. Fig.11 (a) illustrates a triangular MF defined by triangle(x; 3, 6, 8). The trapezoidal MF is specified by four parameters a, b, c, and d as follows:

$$\mu_A(x; a, b, c, d) = \max(\min\left(\frac{x-a}{b-a}, 1, \frac{d-x}{d-b}\right), 0) \quad (15)$$

The parameters *a* and *d* locate the *feet* of the trapezoid and the parameters *b* and *c* locate the *shoulders*. Fig.11 (b) illustrates a trapezoidal MF defined by trapezoid(x; 1, 5, 7, 8). Due to their simple formulas and computational efficiency, both triangular and trapezoidal MFs have been used extensively, especially in real-time implementations. However, since these MFs are composed of straight line segments, they are not smooth at the corner points specified by the parameters.

Gaussian MFs are popular methods for specifying fuzzy sets because of their smoothness and concise notation. These MFs have the advantage of being smooth and nonzero at all points. Gaussian MF is defined by

$$\mu_A(x; c, s) = e^{-\frac{1}{2}\left|\frac{x-c}{s}\right|^2} \quad (16)$$

where *c* is the value of center, and *s* is width of Gaussian curve. Fig.11 (c) illustrates a Gaussian MF defined by Gaussian(x; 2, 5). Although the Gaussian MFs achieve smoothness, they are unable to specify asymmetric membership functions, which are important in certain applications. The sigmoidal MFs are either open left or right. Sigmoidal MF is defined by

$$\mu_A(x; a, c) = \frac{1}{1+ e^{-a(x-c)}} \quad (17)$$

where *c* is the inflection point, and *a* is the slope at *c*. Depending on the sign of the parameter *a*, the sigmoidal membership function is inherently open to the right or to the left. Fig.11 (d) illustrates a sigmoidal MF defined by sigmoid(x; 2, 4).

Summary of Membership Functions:

1. Fuzzy sets describe vague concepts (e.g., fast runner, hot weather, and weekend days).

2. A fuzzy set admits the possibility of partial membership in it. (e.g., Friday is sort of a weekend day, the weather is rather hot).

3. The degree an object belongs to a fuzzy set is denoted by a membership value between 0 and 1. (e.g., Friday is a weekend day to the degree 0.8).

4. A membership function associated with a given fuzzy set maps an input value to its appropriate membership value [47].

IF-THEN rule statements are used to formulate the conditional statements that comprise fuzzy logic. A single fuzzy if-then rule assumes the form:

IF x is A, and y is B then z is C

where A, B and C are linguistic values defined by fuzzy sets on the ranges x, y and z, respectively. The IF-part of the rule "x is A, and y is B" is called the antecedent or premise, while the THEN-part of the rule "z is C" is called the consequent or conclusion.

In fuzzy set theory, the operations, union, intersection, and complement, are defined based on the membership function. The set operations union and intersection correspond to logic operations, disjunction (OR) and conjunction (AND), respectively. The membership function of the union of two fuzzy sets A and B is defined as the maximum of the two individual membership functions:

$$\mu_{\mathrm{A\cup B}}(x) = max\big(\mu_{\mathrm{A}}(x),\mu_{\mathrm{B}}(x)\big) \tag{18}$$

The membership function of the intersection of two fuzzy sets A and B is defined as the minimum of the two individual membership functions:

$$\mu_{A\cap B}(x) = min\left(\mu_A(x),\mu_B(x)\right) \tag{19}$$

The membership function of the complement of a fuzzy set A is defined as the negation of the specified membership function [48]:

$$\mu_{\bar{A}}(x) = 1 - \mu_A(x) \tag{20}$$

3.3.1. Mamdani Fuzzy Inference System (FIS)

The Mamdani FIS used in this study, has eight crisp inputs (F1, F2, F3, F4, F5, F6, F7, and F8) and one crisp output, each having five membership functions as "*very low*", "*low*", "*medium*", "*high*", and "*very high*". All membership functions of the Mamdani FIS system are chosen as Gaussian MF because of being smooth and nonzero at all points.

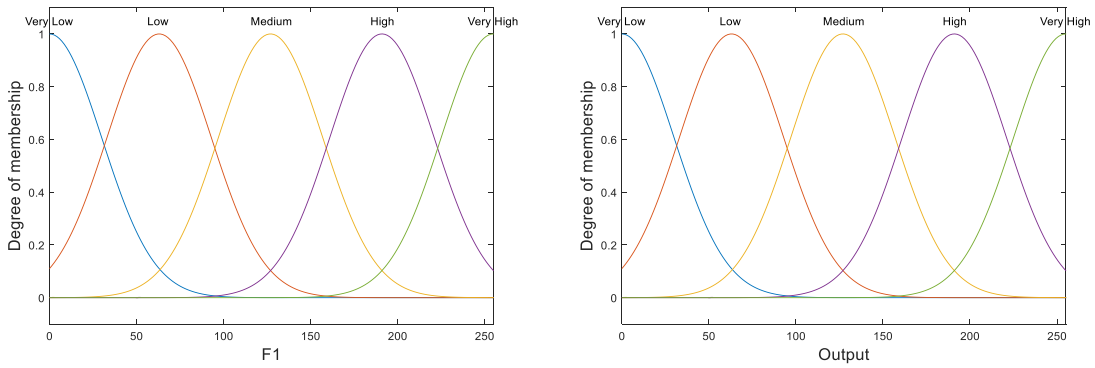

Figure 12 *The membership functions of the first input variable (F1) and output of the fuzzy inference system*

Fig.12 shows the membership functions of one of eight inputs and output variable of the fuzzy inference system. In our system, all membership function parameters are defined as “very low” is Gaussian(x; 30, 0); “low” is Gaussian(x; 30, 63); “medium” is Gaussian(x; 30, 127); “high” is Gaussian(x; 30, 191); and “very high” is Gaussian(x; 30, 255), where Gaussian(x; width, center).

3.3.2. Fuzzy Logic System Rules

Our system has ten rules. First two rules use AND operator, the rest use OR operator. The rules are given in Table.2. As an example, the first rule that used in the fuzzy system is written below:

IF {Input F1 is “*Very Low”*} AND {Input F2 is “*Very Low”*} AND {Input F3 is “Very Low”} AND {Input F4 is “Very Low”} THEN {Output is Very Low}

Table 2 Rules in the Fuzzy Inference System (FIS)

Rule	Input					Operator	Output
		Horizontal (F1 or F5)	Vertical (F2 or F6)	Up Diagonal (F3 or F7)	Down Diagonal (F4 or F8)		
1	Mean	Very Low	Very Low	Very Low	Very Low	AND	Very Low
2	Median	Very Low	Very Low	Very Low	Very Low	AND	Very Low
3	Mean	Low	Low	Low	Low	OR	Low
4	Median	Low	Low	Low	Low	OR	Low

5	Mean	Medium	Medium	Medium	Medium	OR	Medium
6	Median	Medium	Medium	Medium	Medium	OR	Medium
7	Mean	High	High	High	High	OR	High
8	Median	High	High	High	High	OR	High
9	Mean	Very High	Very High	Very High	Very High	OR	Very High
10	Median	Very High	Very High	Very High	Very High	OR	Very High

These rules can be demonstrated with the rule viewer in the system. It is seen in Fig.13, and displays the roadmap of the whole fuzzy inference system. The nine plots across the top of the figure represent the antecedent and consequent of the first rule. Each rule is a row of plots, and each column is a variable. The rule numbers are displayed on the left of each row.

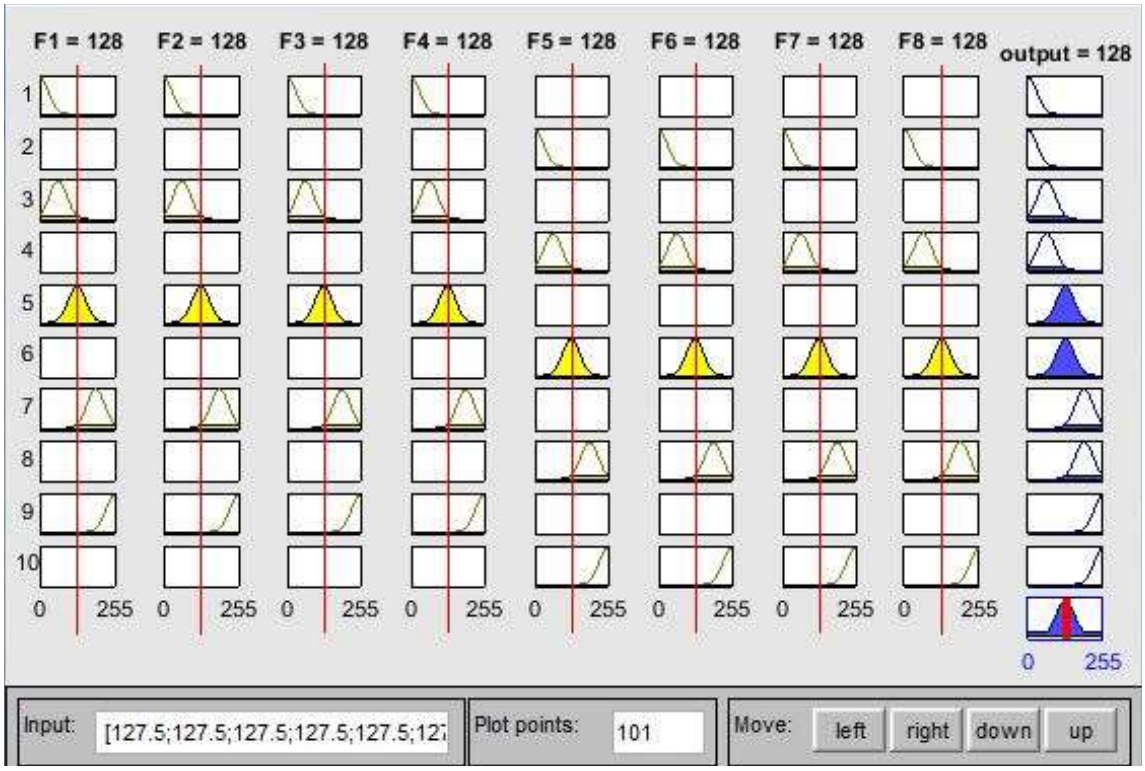

Figure 13 The rule viewer for the fuzzy inference system (FIS)

The first eight columns of plots show the membership functions referenced by the antecedent, or the if-part of each rule. The ninth column of plots shows the membership functions referenced by the consequent, or the then-part of each rule. The eleventh plot in the ninth column of plots represents the aggregate weighted decision for the fuzzy inference system. As an example for F1, it can be said that F1 belongs to *"low"* MF to the degree 0.2 in the third rule, F1 also belongs to *"medium"* MF to the degree 1.0 in the fifth rule, and F1 also belongs to *"high"* MF to the degree 0.2 in the seventh rule.

3.3.3. Evaluation

In this section, all rules are evaluated for features of each pixel in the FOV. Thus, output membership function for corresponding pixel are founded as the union of results of all ten rules. Since the output MF is still a fuzzy set, it is defuzzified into a crisp output by using centroid method. The centroid method is one of the most commonly used defuzzification method and returns the center of the area under the combined output membership function [49]. Fig.14 (a) shows the image (I_{Fuzzy}) after fuzzy logic algorithm was applied.

3.4. Post-processing

The post-processing stage is aimed to obtaining binary image from the fuzzy output image that is still a gray scale image. For each of the 20 images, mean value of I_{NR} normalized image (in the FOV) is individually calculated to set a threshold value for the each corresponding I_{Fuzzy} output of fuzzy images. Eq.21 and Eq.22 illustrate how *Th* value is set.

$$I_{NR_{mean}} = \frac{\sum_{i,j\in FOV}^{M,N} I_{NR}}{\sum_{i,j\in FOV}^{M,N} 1}, \qquad \begin{matrix} i = 1,2,\dots,M \\ j = 1,2,\dots,N \end{matrix} \tag{21}$$

where I_{NR} is the normalized image, M and N are the image size, and i and j are the pixel coordinates in the FOV.

$$Th = \begin{cases} 60, & 19 \le I_{NR_{mean}} \\ 59, & 18 \le I_{NR_{mean}} < 19 \\ 58, & 17 \le I_{NR_{mean}} < 18 \\ 57, & 16 \le I_{NR_{mean}} < 17 \\ 56, & 15 \le I_{NR_{mean}} < 16 \\ 55, & I_{NR_{mean}} < 15 \end{cases} \quad (22)$$

If a pixel value of I_{Fuzzy} is equal or bigger than Th, this corresponding pixel will be classified as vessel (1), otherwise non-vessel (0).

$$I_{Segmented}(i,j) = \begin{cases} 1, & I_{Fuzzy}(i,j) \ge Th \\ 0, & I_{Fuzzy}(i,j) < Th \end{cases} \quad (23)$$

Fig.14 (b) and (c) show segmented image $I_{Segmented}$ and ground truth image, respectively.

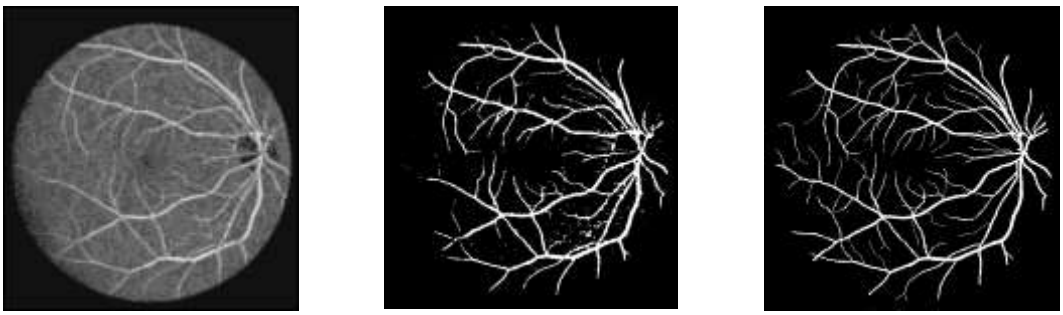

(a) (b) (c)

Figure 14 *(a) I_{Fuzzy}; Output of fuzzy logic algorithm, (b) $I_{Segmented}$; Segmented image, (c) Ground truth image*

CHAPTER 4: RESULTS AND DISCUSSION

4.1. Database

Our method was evaluated with a publicly available retinal image database, DRIVE (Digital Retinal Images for Vessel Extraction) which the images were obtained from a diabetic retinopathy screening program in the Netherlands [50]. 40 eye fundus color images have been randomly selected from 400 diabetic subjects at the program. All images have been taken with a Canon CR5 nonmydriatic 3CCD camera with a 45-degree field-of-view (FOV) and saved as JPEG format. Each image was captured at the image size of 565 by 584 pixels by using 8 bits per color plane. The set of images is divided into two sets; a training set and a test set, both containing 20 images. The training set involves the corresponding FOV masks for the images, which are circular (diameter of approximately 540 pixels) and a single manual segmentation was made by a human observer for each images. The test set also includes the corresponding FOV masks and was manually segmented by two independent human observers, which are accepted as ground truth results. The first observer's segmentation results were used to compare our method results. In order to show differences between two manual segmentations, second observer results are compared with the segmentation of the first observer.

4.2. Performance Measures

The proposed method for the retinal image was evaluated on the images of the DRIVE database. In order to measure the performance of the method, our results were compared with reference to their corresponding hand-drawn ground-truth image. The segmentation accuracy (Acc, the ratio of well-classified pixels), sensitivity (Se, the ratio of well-classified blood vessel pixels), specificity (Sp, the ratio of well-classified non-blood vessel pixels), positive predictive value (Ppv, the ratio of pixels classified as vessel pixel that are correctly classified), and negative predictive value (Npv, the ratio of pixels classified as non-blood vessel pixel that are correctly classified) have been selected as performance measures. These measurements are defined as:

$$Acc = \frac{Tp+Tn}{Tp+Tn+Fp+Fn} \tag{24}$$

$$Se = \frac{Tp}{Tp+Fn} \tag{25}$$

$$Sp = \frac{Tn}{Tn+Fp} \tag{26}$$

$$Ppv = \frac{Tp}{Tp+Fp} \tag{27}$$

$$Npv = \frac{Tn}{Tn+Fn} \tag{28}$$

where Tp (true positive, the number of blood vessels correctly detected), Fn (false negative, the number of blood vessels wrongly detected), Tn (true negative, the number of non-blood vessels correctly detected), and Fp (false positive, the number of non-blood vessels wrongly detected). All these rates are computed considering only pixels inside the

image FOV. Table.3 present the performance results of the proposed method for 20 test images in DRIVE database, while Table.4 shows average, maximum, and minimum of these values.

Table 3 Performance Results on DRIVE Database Images

Image	Acc	Se	Sp	Ppv	Npv	AUC
#1	0.9441	0.7755	0.9698	0.7963	0.9660	0.9631
#2	0.9407	0.7791	0.9695	0.8200	0.9610	0.9584
#3	0.9277	0.7104	0.9654	0.7804	0.9506	0.9417
#4	0.9417	0.7329	0.9744	0.8173	0.9588	0.9348
#5	0.9400	0.6686	0.9835	0.8663	0.9488	0.9376
#6	0.9321	0.6770	0.9748	0.8181	0.9474	0.9241
#7	0.9323	0.6928	0.9696	0.7800	0.9530	0.9329
#8	0.9346	0.6685	0.9732	0.7834	0.9529	0.9273
#9	0.9432	0.6768	0.9795	0.8176	0.9570	0.9387
#10	0.9414	0.6961	0.9753	0.7961	0.9587	0.9377
#11	0.9281	0.7293	0.9584	0.7272	0.9588	0.9328
#12	0.9391	0.7030	0.9737	0.7960	0.9573	0.9416
#13	0.9297	0.6602	0.9751	0.8173	0.9445	0.9323
#14	0.9429	0.7644	0.9671	0.7590	0.9680	0.9576
#15	0.9394	0.7408	0.9628	0.7016	0.9692	0.9424
#16	0.9388	0.7319	0.9707	0.7937	0.9592	0.9500
#17	0.9304	0.7100	0.9619	0.7273	0.9587	0.9267

#18	0.9367	0.7411	0.9627	0.7251	0.9655	0.9416
#19	0.9572	0.8288	0.9752	0.8236	0.9760	0.9612
#20	0.9441	0.7696	0.9655	0.7313	0.9717	0.9548

Table 4 Average, Maximum and Minimum Performance Results on DRIVE Database Images

Image	**Acc**	**Se**	**Sp**	**Ppv**	**Npv**	**AUC**
Ave	0.9382	0.7228	0.9704	0.7839	0.9592	0.9419
Max	0.9572	0.8288	0.9835	0.8663	0.9760	0.9631
Min	0.9277	0.6602	0.9584	0.7016	0.9445	0.9241

The segmented images with the best and the worst case accuracy, Image.19 and Image.03 on DRIVE database, are illustrated in Fig.15, respectively. Average accuracy of 20 images is 0.9382. The best case accuracy is 0.9572 while the worst case is 0.9277.

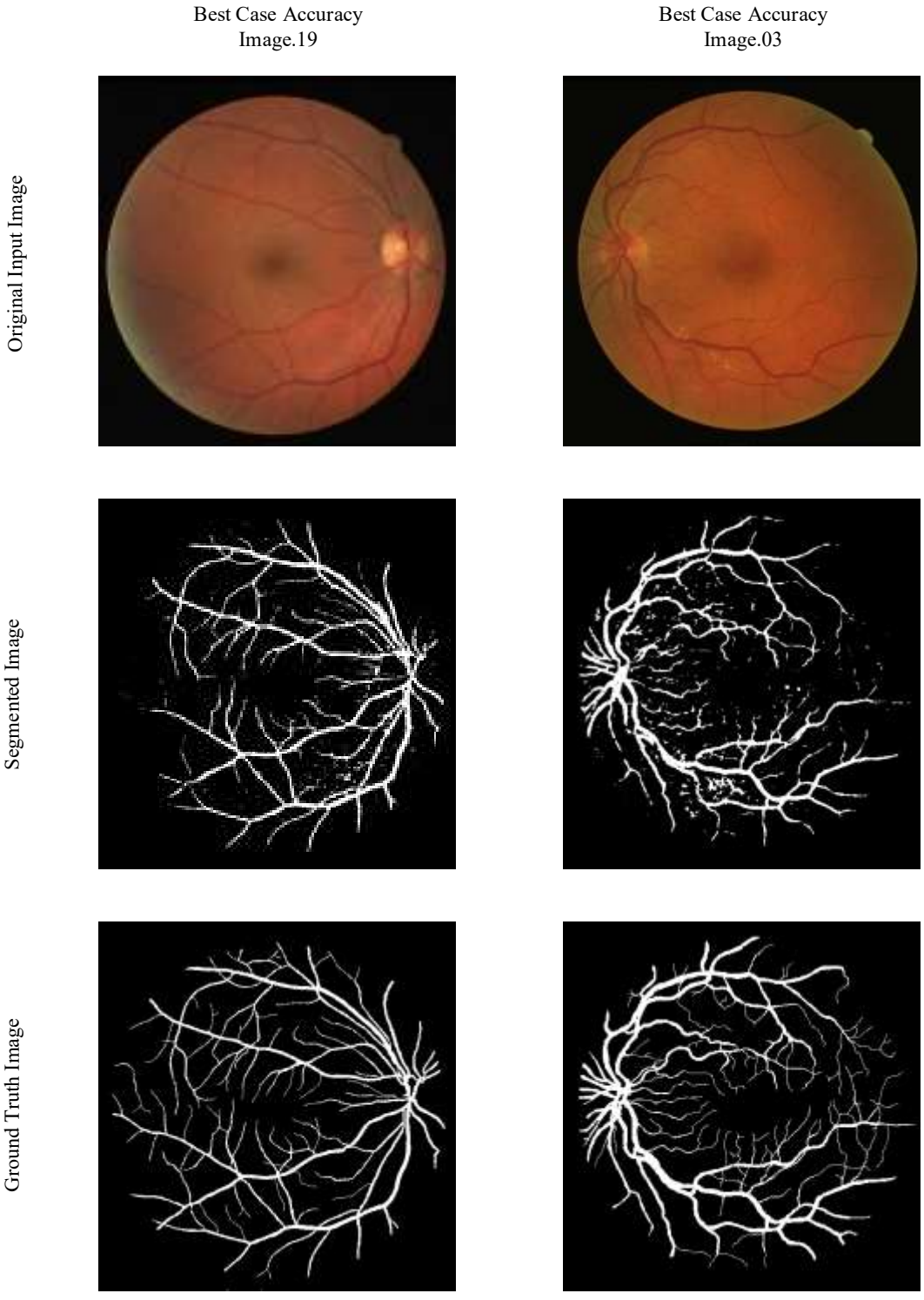

Figure 15 Comparison of the best case and the worst case image segmentation results for accuracy with their original and ground truth image

In addition to these measurements, the receiver operating characteristic (ROC) curve was also plotted and in order to measure the performance of our algorithm. The ROC curve is a plot of true positive fraction (TPF) versus false positive fraction (FPF) by varying the threshold on the probability map. The true positive fraction and the false positive fraction are defined as sensitivity (Se) and specificity (1-Sp), respectively. The closer a curve approaches the top left corner, the better the performance of the system. The value of the area under the ROC curve (AUC), is calculated as a performance measure. It can take values from 0.0 to 1.0 which is for a perfect system. Last columns in Table.3 shows the AUC of each test images while Table.4 shows their average, maximum and minimum. The ROC curve is plotted in Fig.10. This curve is produced by calculating the true and the false positive fraction on all test images through threshold variations. In order to show differences between two ground truths, second observer results are compared with the segmentation of the first observer The plot also shows second observer's hand-drawn segmentation on first observer. TPF is 0.7761, and FPF is 0.0275.

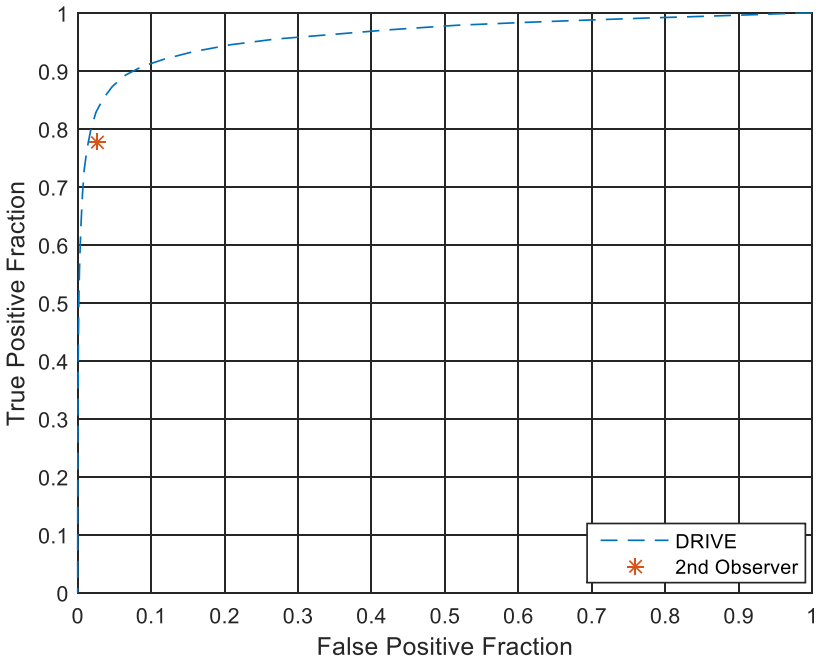

Figure 166 Receiver operating characteristic (ROC) curve for DRIVE database images and second observer segmentation

The segmented images with the best and the worst case AUC, Image.01 and Image.06 on DRIVE database, are illustrated in Fig.17, respectively. Average AUC of 20 images is 0.9419. The best case AUC is 0.9631 while the worst case is 0.9241.

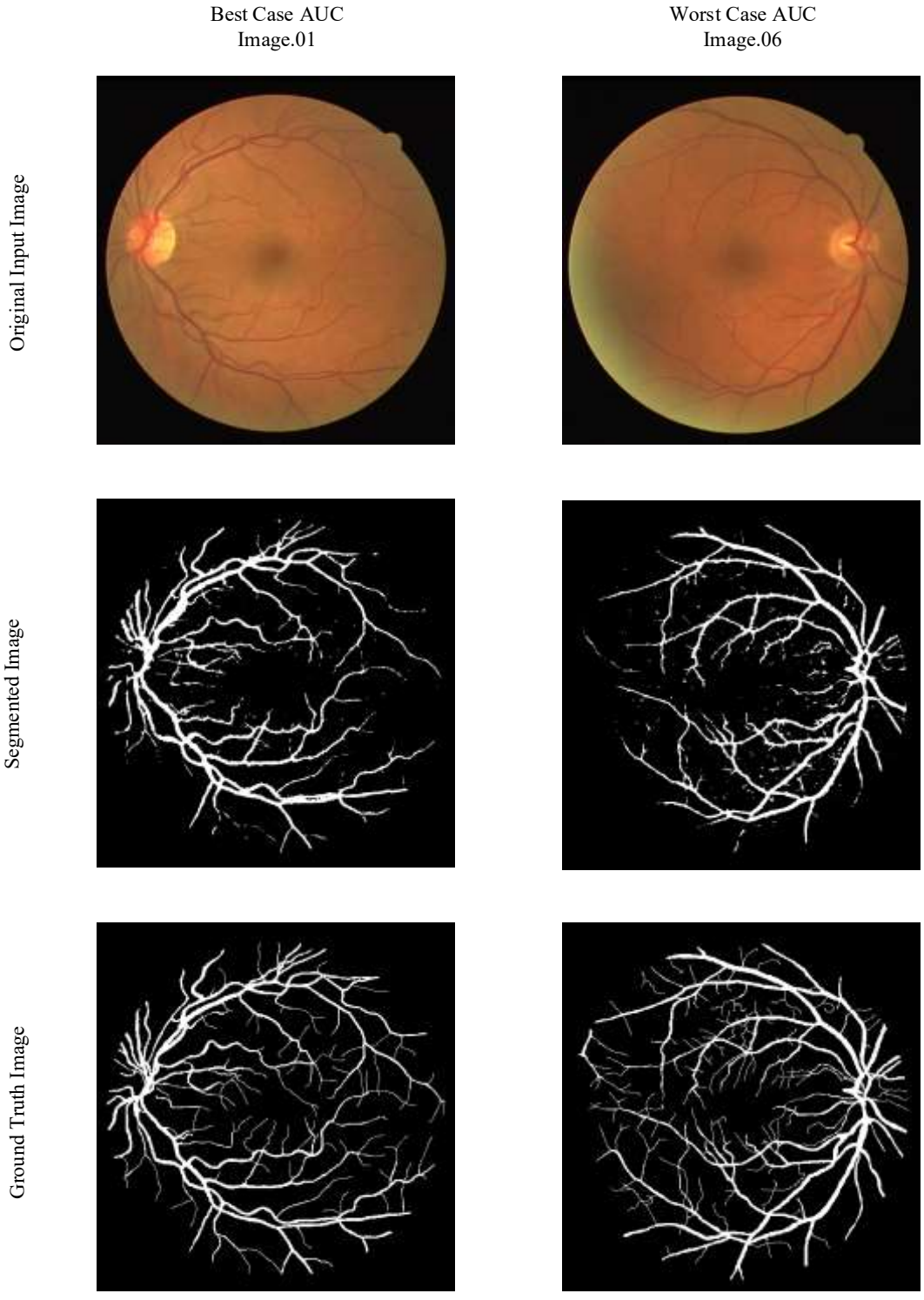

Figure 177 Comparison of the best case and the worst case image segmentation results for AUC with their original and ground truth image

4.3. Comparison to Other Methods

The performance of our algorithm is compared with other well-known retinal vessel segmentation algorithms published in the past years. Since the accuracy (Acc) and area under ROC curve (AUC) measurements were provided by other authors, these measurements were computed in our method as well. Table.5 shows chronologically performance results in terms of type, average accuracy and AUC for the DRIVE database with the following published methods: Chaudhuri *et al.* [16], Jiang and Mojon [20], Niemeijer *et al.* [25], Staal *et al.* [26], Mendonça *et al.* [13], Soares *et al.* [28], Martinez-Perez *et al.* [21], Ricci and Perfetti [29], Cinsdikici and Aydin [17], Marin *et al.* [31], Li *et al.* [18], Fraz *et al.* [32], and Isam *et al.* [36]. All these rule-based and supervised methods have been stated in Literature Survey section. The values shown in Table.5 are presented by their authors. If they are not available, they were not included in the tables, thus appearing as a dash (-).

Table 5 *Performance Results Compared to Other Methods on the Drive Database in Terms of Type, Average Accuracy and Area under ROC Curve (AUC)*

Methods	Type	Year	Acc	AUC
2nd observer	-	-	0.9473	-
Chaudhuri *et al.* [16]	Rule-based	1989	0.8773	0.7878
Jiang and Mojon [20]	Rule-based	2003	0.8911	0.9327
Niemeijer *et al.* [25]	Supervised	2004	0.9416	0.9294
Staal *et al.* [26]	Supervised	2004	0.9441	0.9520

Mendonça *et al.* [13]	Rule-based	2006	**0.9463**	-
Soares *et al.* [28]	Supervised	2006	0.9466	0.9614
Martinez-Perez [21]	Rule-based	2007	0.9344	-
Ricci and Perfetti [29]	Supervised	2007	**0.9595**	0.9633
Cinsdikici and Aydin [17]	Rule-based	2009	0.9293	0.9407
Marin *et al.* [31]	Supervised	2011	0.9452	0.9588
Li *et al.* [18]	Rule-based	2012	0.9343	-
Fraz *et al.* [32]	Supervised	2012	0.9480	**0.9747**
Isam *et al.* [36]	Rule-based	2015	0.9402	0.8762
This methods	Rule-based	2015	0.9382	**0.9419**

It is important to point out that supervised methods often outperform rule-based methods. However, supervised methods may show significant performance loss when applied to a different database. All compared supervised methods achieved slightly higher accuracy rates than our method. Among all methods, Ricci and Perfetti [29] provided the best performance accuracy (95.95%). Nevertheless, the accuracy of our algorithm exceeds the most of the previous rule-based methods. Our method achieved an accuracy rate of 93.82% for the DRIVE databases. It is outperformed by Mendonça *et al.* [13] (94.63%) and Isam *et al.* [36] (94.02%) among rule-based method. Our results also demonstrated a sensitivity of 72.28% and a specificity of 97.04% for the DRIVE database. According to these results, the method is suitable for pixel classification as vessel or non-vessel.

Another important measure of the performance of a method is the area under the ROC curve (AUC). In terms of AUC, our proposed method reaches the highest area (0.9419) than among rules-based methods, and also better performance than Niemeijer et al. [25] as a supervised method. Mendonca et al. [13], Martinez-Perez [21] and Li *et al.* [18] did not report their AUC values. 0.9419 AUC was achieved for the DRIVE databases.

CHAPTER 5: CONCLUSION

Previous methods for blood vessel segmentation in retinal images can be classified into two group: rule-based and supervised methods. This study proposes a new rule-based vessel classification method using a fuzzy logic algorithm. In recent years, the use of fuzzy logic technique has been a very popular method in many areas such as control systems, robotics and noise recognition algorithms. It can also be successful in the area of image processing. However there is no specific fuzzy method for the retinal vessel segmentation in the literature.

Feature parameters derived from experimentally measured (mean and median the feature vectors -pixel itself, first and second nearest neighbor- are calculated at four directions: horizontal, vertical, up diagonal, and down diagonal) were used to develop a fuzzy logic system for segmenting retinal vessel.

The performance of our method is tested by using the DRIVE databases as the previous studies in the literature. Our method achieved accuracy rates (93.82%) and highest area under curve (0.9419) among rule-based methods. The results demonstrate that our algorithm outperforms other methods and approximates the average accuracy of a human observer without a significant degradation of sensitivity and specificity. The total processing time of a single image is less than 3 minutes, running on a PC with an Intel(R) Core(TM) 2 CPU at 1.80 GHz and 3 GB of RAM.

The drawback of the proposed system is that it is missing vessels of small diameter and low contrast. The diameter of a vessel decreases as it travels radially outward from the optic disk.

Its effectiveness and robustness with different image conditions, together with its simplicity and fast implementation, make this blood vessel segmentation proposal suitable for retinal image computer analyses such as automated screening for early diabetic retinopathy detection. The performance of the method could be improved by adding new features or linguistic rules.

REFERENCES

[1] Abràmoff, Michael D., Mona K. Garvin, and Milan Sonka. "Retinal imaging and image analysis." *IEEE reviews in biomedical engineering* 3 (2010): 169-208.

[2] https://www.nei.nih.gov/health/diabetic/retinopathy

[3] Tang, Johnny, and Timothy S. Kern. "Inflammation in diabetic retinopathy." *Progress in retinal and eye research* 30.5 (2011): 343-358.

[4] http://arleoeye.com

[5] Davidson, Jaime A., Thomas A. Ciulla, Janet B. McGill, Keri A. Kles, and Pamela W. Anderson. "How the diabetic eye loses vision." *Endocrine* 32.1 (2007): 107-116.

[6] Ciulla, Thomas A., Armando G. Amador, and Bernard Zinman. "Diabetic retinopathy and diabetic macular edema." *Diabetes Care* 26 (2003): 2653-2664.

[7] Bressler, Neil M., Susan B. Bressler, and Stuart L. Fine. "Age-related macular degeneration." *Survey of ophthalmology* 32.6 (1988): 375-413.

[8] https://www.nei.nih.gov/health/maculardegen/armd_facts

[9] http://pixgood.com/age-related-macular-degeneration.html

[10] Kawasaki, Ryo, Jie Jin Wang, Elena Rochtchina, Anne J. Lee, Tien Yin Wong, and Paul Mitchell. "Retinal vessel caliber is associated with the 10-year incidence of glaucoma: the Blue Mountains Eye Study." *Ophthalmology* 120.1 (2013): 84-90.

[11] http://www.aao.org/newsroom/release/20130102.cfm

[12] http://octulsa.com/services/glaucoma

[13] Mendonca, Ana Maria, and Aurelio Campilho. "Segmentation of retinal blood vessels by combining the detection of centerlines and morphological reconstruction." *Medical Imaging, IEEE Transactions on* 25.9 (2006): 1200-1213.

[14] Gagnon, Langis, Marc Lalonde, Mario Beaulieu, and Marie-Carole Boucher. "Procedure to detect anatomical structures in optical fundus images." *Medical Imaging 2001*. International Society for Optics and Photonics, (2001): 1218-1225.

[15] Can, Ali, Hong Shen, James N. Turner, Howard L. Tanenbaum, and Badrinath Roysam. "Rapid automated tracing and feature extraction from retinal fundus images using direct exploratory algorithms." *Information Technology in Biomedicine, IEEE Transactions on* 3.2 (1999): 125-138.

[16] Chaudhuri, Subhasis, Shankar Chatterjee, Norman Katz, Mark Nelson, and Michael Goldbaum. "Detection of blood vessels in retinal images using two-dimensional matched filters." *IEEE Transactions on medical imaging* 8.3 (1989): 263-269.

[17] Cinsdikici, Muhammed Gökhan, and Doğan Aydın. "Detection of blood vessels in ophthalmoscope images using MF/ant (matched filter/ant colony) algorithm." *Computer methods and programs in biomedicine* 96.2 (2009): 85-95.

[18] Li, Qin, Jane You, and David Zhang. "Vessel segmentation and width estimation in retinal images using multiscale production of matched filter responses." *Expert Systems with Applications* 39.9 (2012): 7600-7610.

[19] Heneghan, Conor, John Flynn, Michael O'Keefe, and Mark Cahill. "Characterization of changes in blood vessel width and tortuosity in retinopathy of prematurity using image analysis." *Medical image analysis* 6.4 (2002): 407-429.

[20] Jiang, Xiaoyi, and Daniel Mojon. "Adaptive local thresholding by verification-based multithreshold probing with application to vessel detection in retinal images." *Pattern Analysis and Machine Intelligence, IEEE Transactions on* 25.1 (2003): 131-137.

[21] Martinez-Perez, M. Elena, Alun D. Hughes, Simon A. Thom, Anil A. Bharath, and Kim H. Parker. "Segmentation of blood vessels from red-free and fluorescein retinal images." *Medical image analysis* 11.1 (2007): 47-61.

[22] Tolias, Yannis A., and Stavros M. Panas. "A fuzzy vessel tracking algorithm for retinal images based on fuzzy clustering." *Medical Imaging, IEEE Transactions on* 17.2 (1998): 263-273.

[23] Rahman, R., SM Raiyan Kabir, and Anita Quadir. "Application of fuzzy inference and active contour model for detection of fovea and its center in a fundus image." *Signal, Image and Video Processing* (2015): 1-8.

[24] Köse, Cemal, and Cevat İki. "A personal identification system using retinal vasculature in retinal fundus images." *Expert Systems with Applications* 38.11 (2011): 13670-13681.

[25] Niemeijer, Meindert, Bram van Ginneken, Joes Staal, Maria SA Suttorp-Schulten, and Michael D. Abràmoff. "Automatic detection of red lesions in digital color fundus photographs." *Medical Imaging, IEEE Transactions on* 24.5 (2005): 584-592.

[26] Staal, Joes, Michael D. Abràmoff, Meindert Niemeijer, Max A. Viergever, and Bram van Ginneken. "Ridge-based vessel segmentation in color images of the retina." *Medical Imaging, IEEE Transactions on* 23.4 (2004): 501-509.

[27] Sinthanayothin, Chanjira, James F. Boyce, Helen L. Cook, and Thomas H. Williamson. "Automated localisation of the optic disc, fovea, and retinal blood vessels from digital colour fundus images." *British Journal of Ophthalmology* 83.8 (1999): 902-910.

[28] Soares, João VB, Jorge JG Leandro, Roberto M. Cesar, Herbert F. Jelinek, and Michael J. Cree. "Retinal vessel segmentation using the 2-D Gabor wavelet and supervised classification." *Medical Imaging, IEEE Transactions on* 25.9 (2006): 1214-1222.

[29] Ricci, Elisa, and Renzo Perfetti. "Retinal blood vessel segmentation using line operators and support vector classification." *Medical Imaging, IEEE Transactions on* 26.10 (2007): 1357-1365.

[30] Gardner, G. G., D. Keating, T. H. Williamson, and A. T. Elliott. "Automatic detection of diabetic retinopathy using an artificial neural network: a screening tool." *British journal of Ophthalmology* 80.11 (1996): 940-944.

[31] Marín, Diego, Arturo Aquino, Manuel Emilio Gegúndez-Arias, and José Manuel Bravo. "A new supervised method for blood vessel segmentation in retinal images by using gray-level and moment invariants-based features." *Medical Imaging, IEEE Transactions on* 30.1 (2011): 146-158.

[32] Fraz, Muhammad Moazam, Paolo Remagnino, Andreas Hoppe, Bunyarit Uyyanonvara, Alicja R. Rudnicka, Christopher G. Owen, and Sarah A. Barman. "An ensemble classification-based approach applied to retinal blood vessel segmentation." *Biomedical Engineering, IEEE Transactions on* 59.9 (2012): 2538-2548.

[33] Walter, Thomas, Pascale Massin, Ali Erginay, Richard Ordonez, Clotilde Jeulin, and Jean-Claude Klein. "Automatic detection of microaneurysms in color fundus images." *Medical image analysis* 11.6 (2007): 555-566.

[34] Pizer, Stephen M., E. Philip Amburn, John D. Austin, Robert Cromartie, Ari Geselowitz, Trey Greer, Bart ter Haar Romeny, John B. Zimmerman, and Karel

Zuiderveld. "Adaptive histogram equalization and its variations." *Computer vision, graphics, and image processing* 39.3 (1987): 355-368.

[35] Hossain, Foisal, and Mohammad Reza Alsharif. "Image enhancement based on logarithmic transform coefficient and adaptive histogram equalization." *Convergence Information Technology, 2007. International Conference on*, pp. 1439-1444. IEEE, 2007.

[36] Isam S. Hameed, Helen Ocbagabir, Buket D. Barkana, and Burak Yildirim. "Blood Vessel Segmentation in Retinal Images by Morphological Operations and by a Novel Pixel Tracking Algorithm." *International journal of innovative computing, information & control: IJICIC*, 11.1(2015): 189-201.

[37] Thapar, Suman, and Shevani Garg. "Study and Implementation of Various Morphology Based Image Contrast Enhancement Techniques." *International Journal of Computing & Business Research ISSN (Online)* (2012): 2229-6166.

[38] Hosking, Jonathan Richard Morley, and James R. Wallis. *Regional frequency analysis: an approach based on L-moments*. Cambridge University Press, 2005.

[39] Zadeh, Lotfi A. "Fuzzy sets." *Information and control* 8.3 (1965): 338-353.

[40] Uzkent, Burak, Buket D. Barkana, and Jidong Yang. "Automatic environmental noise source classification model using fuzzy logic." *Expert Systems with Applications* 38.7 (2011): 8751-8755.

[41] Kerre, Etienne E., and Mike Nachtegael, eds. *Fuzzy techniques in image processing*. Vol. 52. Springer Science & Business Media, 2000.

[42] Wang, L-X., and Jerry M. Mendel. "Fuzzy basis functions, universal approximation, and orthogonal least-squares learning." *Neural Networks, IEEE Transactions on* 3.5 (1992): 807-814.

[43] Russo, Marco, and Lakhmi C. Jain. *Fuzzy learning and applications*. CRC Press, 2000.

[44] Takagi, Tomohiro, and Michio Sugeno. "Fuzzy identification of systems and its applications to modeling and control." *Systems, Man and Cybernetics, IEEE Transactions on* 1 (1985): 116-132.

[45] Mamdani, Ebrahim H., and Sedrak Assilian. "An experiment in linguistic synthesis with a fuzzy logic controller." *International journal of man-machine studies* 7.1 (1975): 1-13.

[46] Jang, J. S. R., C. T. Sun, and E. Mizutani. "Neuro-fuzzy and soft computing. 1997." *PTR Prentice Hall* (1997).

[47] http://www.mathworks.com/help/fuzzy

[48] Maimon, Oded, and Lior Rokach, eds. *Data mining and knowledge discovery handbook*. Vol. 2. New York: Springer, 2005.

[49] Castro, Juan Luis. "Fuzzy logic controllers are universal approximators." *Systems, Man and Cybernetics, IEEE Transactions on* 25.4 (1995): 629-635.

[50] Research Section, Digital Retinal Image for Vessel Extraction, (DRIVE) Database. Utrecht, the Netherlands, Univ., Med. Center Utrecht, Image Sci. Inst. [Online]. Available: http://www.isi.uu.nl/Research/Databases/DRIVE